Nanoscale

Accepted Manuscript

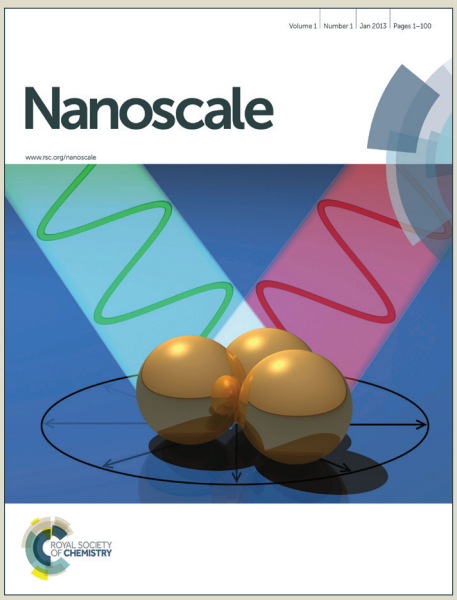

ROYAL SOCIETY OF CHEMISTRY

www.rsc.org/nanoscale

Nanoscale

ARTICLE

Dynamic imaging of single gold nanoparticle in liquid irradiated by off-resonance femtosecond laser

Received 00th January 20xx,
Accepted 00th January 20xx

DOI: 10.1039/x0xx00000x

www.rsc.org/

Christos Boutopoulos[a], Ali Hatef[b], Matthieu Fortin-Deschênes[a] and Michel Meunier[a*]

Plasmonic nanoparticles can lead to extreme confinement of the light in the near field. This unique ability of plasmonic nanoparticles can be used to generate nanobubbles in liquid. In this work, we demonstrate with single-particle monitoring that 100 nm gold nanoparticles (AuNPs) irradiated by off-resonance femtosecond (fs) laser in the tissue therapeutic optical window (λ = 800 nm), can act as a durable nanolenses in liquid and provoke nanocavitation while remaining intact. We have employed combined ultrafast shadowgraphic imaging, *in-situ* dark field imaging and dynamic tracking of AuNP Brownian motion to ensure the study of individual AuNPs/nanolenses under multiple fs laser pulses. We demonstrate that 100 nm AuNPs can generate multiple, highly confined (radius down to 550 nm) and transient (life time < 50 ns) nanobubbles. The latter is of significant importance for future development of *in-vivo* AuNP-assisted laser nanosurgery and theranostic applications, where AuNP fragmentation should be avoided to prevent side effects, such as cytotoxicity and immune system's response. The experimental results have been correlated with theoretical modeling to provide an insight to the AuNP-safe cavitation mechanism as well as to investigate the deformation mechanism of the AuNPs at high laser fluences.

Introduction

The unprecedented ability of plasmonic nanoparticles (NPs) to concentrate light to deep sub-wavelength volumes has propelled their use in several laser cell nanosurgery applications. These include cancer photothermal therapy as well as the creation of transient pores in a living cell's membrane, which open up applications such as drug delivery and cell transfection[1–5]. Plasmonic NP assisted cell nanosurgery is facilitated by transient sub-micron bubbles generated in close proximity to cells due to NPs excitation. Bubble generation and evolution strongly depends on the laser parameters such as pulse duration, wavelength and fluence[1,6–9]. In particular, bubble generation has been mainly associated to NP heating and vaporization of the surrounding liquid when on-resonance laser irradiation is used[1,10]. On-resonance laser irradiation (i.e. on-resonance peak wavelength 579 nm for 100 nm gold NP (AuNP)) maximizes the laser pulse energy absorption by the NPs due to their high absorption cross section. Recently, we proposed a nanoplasma mediated bubble generation mechanism for laser cell nanosurgery applications based on off-resonance femtosecond (fs) laser excitation (wavelength 800 nm) of plasmonic AuNPs[7,11]. In the off-resonance excitation, the energy absorption by the AuNPs is minimized due to their low absorption cross section. The nanoplasma generation occurs in the vicinity of the AuNP due to the near-field enhancement (nanolens effect[12]) and the photoionization efficiency of the fs pulses.

Plasmonic bubble (PB) detection and more importantly PB *in-situ* monitoring allows for understanding the cell nanosurgery mechanism as well as for processing optimization. Therefore, due to their crucial role in cell nanosurgery, PB generation around pulsed laser excited plasmonic NPs is receiving growing interest by several research groups[13–17]. Due to their transient and confined nature, PB studies demand the development of detection methods with nanoscale temporal and spatial resolution. To that aim, researchers employ a variety of techniques[1,13] to either perform PB detection or investigate PB dynamics, including: (a) time-resolved X-ray scattering[15] (b) photodiode assisted electrical detection of PB dynamics by means of optical scattering of a continuous wave probe beam[1,13,14] and (c) acoustic detection with ultrasound transducers[13]. Time-resolved X-ray scattering allows for excellent spatial and temporal precision up to tenths of nm and few ps, respectively. However, the technique is limited by the experimental complexity arising from the need to probe PB

[a] Laser Processing and Plasmonics Laboratory, Engineering Physics Department, Polytechnique Montréal, Montréal, Québec H3C 3A7, Canada
[b] Nipissing Computational Physics Laboratory, Department of Computer Science and Mathematics, Nipissing University, North Bay, Ontario, P1B 8L7, Canada

† Additional supporting information may be found in the online version of this article at the publisher's website. The **supplementary video 1** shows successive transient bubbles generated by fs laser excitation of a dynamic pair of AuNP at F_{peak} = 200 mJ/cm^2. Both the camera frame rate and the fs laser repetition rate where synchronized at 10 Hz. The pump-prop delay was set to 10 ns. **The supplementary video 2** shows the complete dynamic evolution of a transient nanobubble generated around a single AuNP/nanolens, following fs laser excitation at F_{peak} = 200 mJ/cm^2.

using X-ray synchrotron irradiation. The indirect principle of detection of the above studies involves excitation of several NP or NP clusters within the laser beam focal volume. As a result, the detected signal cannot be linked to single NP/PB events with reliability. Indeed, strong scattering of the probe beam from large PBs, generated by either NP clusters or interfering PBs will dominate the measured signal.

Pump-probe imaging methods enable single PB detection. In fact, charge-coupled devices (CCD) have been used for single AuNP/PB detection by means of time delayed scattering of a ns probe[10,13,18] or time delayed shadowgraphy[16]. The combined use of the two detection schemes has been employed by Vogel et al.[19] for fs nanocavitation studies in water and by Lapotko group[20] for PB detection, allowing for increased spatial and temporal resolution. So far, those techniques have not been combined to monitor single NP motion and PB generation and/or to demonstrate the response of a single NP under multiple pulses. Therefore, despite the large amount of studies dealing with PB detection, significant aspects concerning to either PB detection or more importantly NPs efficiency in multiple PB generation remain unclear. These include (a) the direct study of the NPs state following laser excitation, PB generation and collapse (b) the definition of NPs ability to generate multiple successive PB, and (c) the *in-situ* definition of the NPs deformation threshold using a direct and reliable single NP approach. The latter is of significant importance when considering *in-vivo* nanosurgery applications, where NP fragmentation should be avoided to prevent side effects of the fragments on the cells such as cytotoxicity and endocytosis[21].

In this work, we apply a shadowgraphic dynamic imaging technique to study the response of AuNPs under off-resonance fs laser excitation. The key advantage of this approach is the possibility to perform a dynamic study while tracking a single AuNP under multiple fs pulses with nanoscale spatial and temporal resolution. Ultrafast PB dynamics have been observed and analyzed revealing that AuNPs generate a strong nanolens effect in liquid. The AuNP tolerance under various laser fluences has been examined *in-situ* with dark field microscopy. Furthermore, we employed the two temperature model (TTM) to correlate the experimental results with the key physical phenomena involved in the interaction of the fs laser irradiation with the AuNP (i.e. thermodynamic response of the AuNP, near-field enhancement at the poles of the particle and nanoplasma generation).

Experimental

Preparation of the AuNP sample

A drop of 30 μL AuNP solution (Nanopartz A11-100) was first deposited on the cover slip bottom of a petri dish (MatTek) and then capped with a second cover slip. As a result, a sealed container of ~ 0.05 cm^3 was formed between the two cover slips separated by the plastic bottom support of the petri dish (see Fig. 1). In order to ensure single AuNP tracking we selected a low concentration AuNP solution (1.7 x 10^8 NP/cm^3).

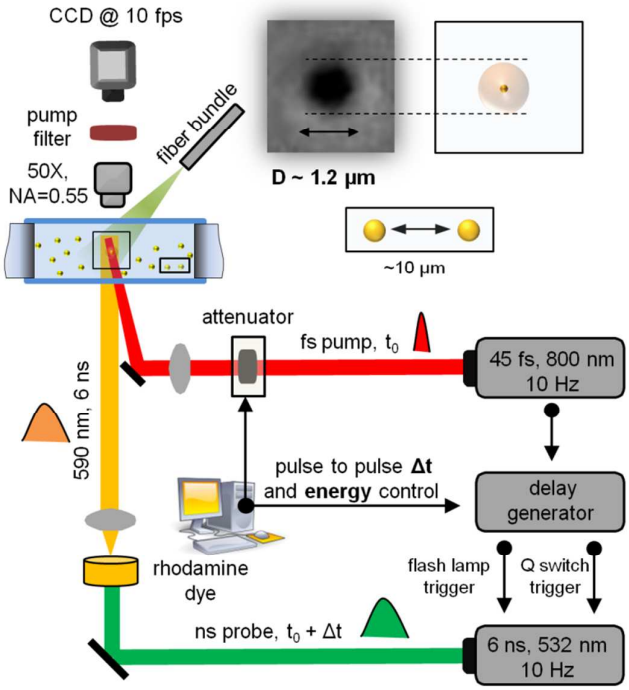

FIGURE 1: Experimental setup for dynamic tracking of fs laser-induced bubbles around single AuNPs. The optical setup allows for submicron spatial resolution while the electronic synchronization allows for ~ 1 ns temporal resolution at 10 Hz capturing repetition rate. The inset shows an indicative shadowgraphic image of a ~ 1.2 μm bubble captured 20 ns after its generation around a single AuNP.

The mean distance between the AuNPs was calculated to be ~ 10 μm by using the theoretical formulation described in Ref[22].

Femtosecond laser excitation

A Ti:Sapphire laser (6 mJ/pulse, 45 fs, 800 nm, 1 kHz, Spitfire from Spectra-Physics) was used for the irradiation of the AuNPs. The linear polarized beam was focused at the middle plane of the container using a long focal length lens (f = 750 mm). A Gaussian beam profile was measured with a spot diameter of 0.5 mm (defined at $1/e^2$). Dynamic tracking of single AuNP/PB dynamics was performed in the central part of the spot. Therefore, we considered the peak fluence at the center of the Gaussian spot (twice the average fluence) for our analysis. This has to be taken into account when correlating our results with cell manipulation studies where the average laser fluence is usually reported. The beam was slightly tilted regarding to the imaging axis to prevent the direct exposure of the optical elements and the CCD camera (IMI Teck IMB-17FT) to fs pulses.

Ultrafast pump-probe imaging

The ultrafast dynamics involved in the generation of bubbles around plasmonic NPs cannot be captured by conventional high speed cameras. Therefore, an ultrafast pump-probe imaging shadowgraphic setup was used (Fig. 1). The setup was based on the electronic synchronization of the fs laser (pump)

with a nanosecond (ns) laser (probe) (Quantel) at 10 Hz. The electronics allowed for ~1 ns temporal synchronization resolution. More importantly, the electronic control of the setup offered a module for pulse-to-pulse alteration of either the delay or the laser fluence. These functions allowed for investigating PB and the AuNP deformation by capturing the response of single AuNP (i.e., always the same AuNP) under various experimental conditions. Note that the ns probe pulses (λ = 532 nm, τ = 6 ns) were first directed to excite a fluorescence dye (rhodamine) solution. The technique allows for high quality imaging due to the emission of incoherent light from the dye (broad peak centered around 590 nm, τ ~ 6 ns). A long working distance 50X objective lens (Mitutoyo, NA = 0.55) was used for the imaging. The selection of the objective was a compromise in terms of spatial resolution (0.61 λ/NA ~ 650 nm) and relatively long depth of focus (~ 1 µm). The latter is crucial for extending the maximum tracking time of a single AuNP. Indeed, due to Brownian motion, a AuNP typically moves by few µm during 1s and thus remains in the depth of focus of the imaging system for sufficient time to perform measurements.

Dark field imaging

Continuous illumination (halogen lamp) was appropriately adapted sidelong to the AuNP solution container using a fiber light guide (see Fig. 1). The light scattered from the sample allowed for dark field (DF) imaging of the AuNPs Brownian motion. For *in-situ* AuNP deformation measurements, the pump laser repetition rate was 10 Hz and DF pictures were captured at 5 Hz.

Single AuNP PB dynamics

A protocol of three steps was followed in order to ensure imaging and study of bubble dynamics around a single AuNP: (a) the two optical systems (i.e. fs pump beam delivery and imaging system) were adjusted to be on focus in the middle plane of the sealed container, where the probability to find AuNP clusters is extremely low, (b) the 100 nm diameter of the floating NPs in the focusing plane was periodically confirmed using the DF module and the Brownian motion formulation[23], (c) the concentration of the solution was selected to result in a ~ 10 µm mean distance between the NPs. Therefore, the interference between neighboring bubbles was minimized and well discriminated from single bubble events (see Fig. 2b and 2c).

Image processing

Sequences of images (10 to 30) were captured at 10 Hz using a pulse-to-pulse alteration of either the pump-probe delay or the laser fluence. The image sequences were analyzed using the ImageJ software to extract the bubble sizes. Slight contrast enhancement and brightness correction were applied. Note that ~ 20 % of the total AuNPs initially appeared in the imaging field remained traceable during the whole capturing time (i.e., considered as successful events). During the PB imaging process some AuNPs moved out of the imaging plane resulting in relatively blur PB images. The latter had no effect on single AuNP/PB studies since tracking of particles was not lost. Only sharp images, considered in focus, where analyzed to extract PB size. More than 5 successful events were averaged to analyze the PB dynamics.

Results and Discussion

Evaluation of the dynamic imaging system

Towards the evaluation of the detection method, the initial experimental work emphasized to the detection of multiple PB generated around single AuNPs. A typical experiment of multiple PB detection around single AuNPs excited with 200 mJ/cm^2 fs irradiation is presented in **supplementary video 1**. Submicron bubbles could be efficiently detected when their z position, which varies with time due to NP Brownian motion, lies within the depth of focus of the imaging system. Figure 2 depicts a representative series of pump-probe frames extracted from the **supplementary video 1** revealing PB generation by a dynamic pair of AuNPs. In the three first frames of Figure 2 (first row), two single AuNPs generate discrete PB (~1 µm), while in the late three frames (second row) we observe *in-situ* the formation of a NP dimmer from the initial pair of the AuNPs. The dimmer excitation results in larger PB (~2 µm). It is mentioned that pump-probe pictures were taken at a fixed delay of 10 ns. In this time scale PB generated by single AuNP gain size of about 1 µm.

PB dynamics generated by a single AuNP/nanolens

Following the initial evaluation process, we studied PB dynamics generated by fs excitation of 100 nm AuNPs under different peak laser fluence F_{peak} conditions, namely 150 mJ/cm^2, 200 mJ/cm^{2}and 250 mJ/cm^2. The selection of the specific parameters was based on our recent work[24], where fs

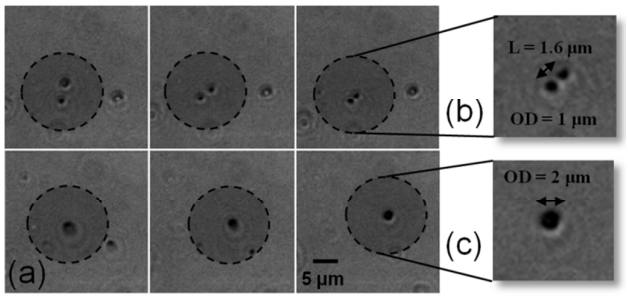

FIGURE 2 a) Dynamic tracking of pair of AuNP generating successive bubbles under fs irradiation at peak fluence F_{peak} = 200 mJ/cm^2 (extracted from supplementary video 1). The formation of dimmer of AuNPs can been observed *in situ* : the initially discrete AuNPs (first row) form a dimmer (second row) b) Close up of a pair of PB (~ 1 µm in diameter), generated by 2 single AuNPs, separated by ~ 1.6µm. c) Close up of a ~ 2 µm PB generated by a dimmer of AuNPs. Imaging and fs excitation repetition rate were synchronized at 10 Hz. The pump-probe delay was 10 ns. L stands for inter-particle distance and OD for diameter.

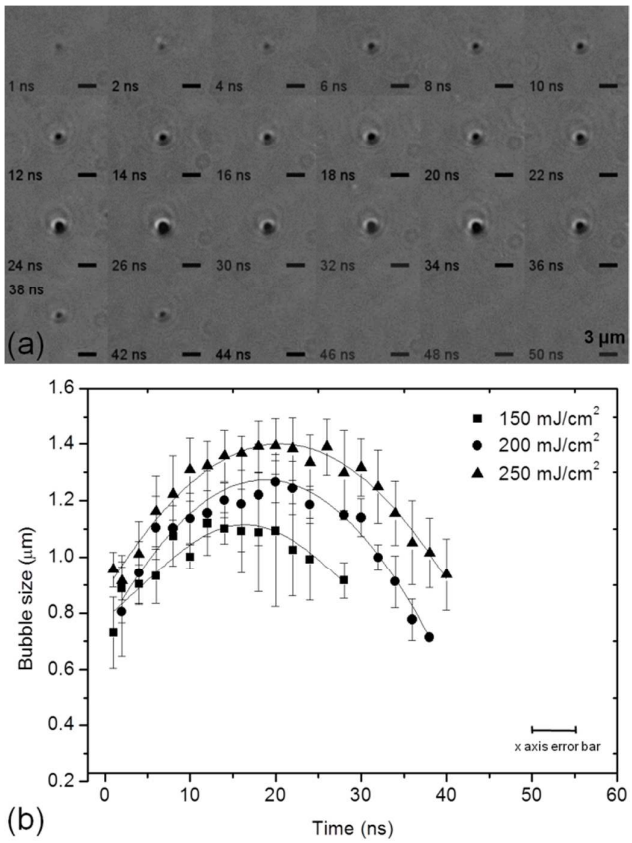

FIGURE 3: a) A series of time-resolved shadowgraphic images of successive bubbles generated by fs laser excitation of a single plasmonic AuNP at F_{peak} = 200 mJ/cm^2. Images were captured at 10 Hz with a 2 ns pulse-to-pulse increase of the pump-probe delay. Two dimensional movement of the particle was corrected by using image processing software. b) Measured bubble diameter as a function of time for F_{peak} = 150 mJ/cm^2, 200 mJ/cm^2 and 250 mJ/cm^2. The bubble size error bars correspond to the standard deviation of 5 successful events (i.e., complete bubble dynamics tracking around 5 different NPs).

irradiation of 100 nm AuNPs under a similar laser fluence range resulted in efficient perforation and transfection of cancer cells. Notice that average fluence $F_{average}$ is considered in ref[24], as in most of the NP assisted laser cell treatment works. In our work, peak laser fluence F_{peak} is always considered since AuNPs are monitored at the central part of the laser beam, having a Gaussian spatial distribution. For this spatial profile, one can deduce that $F_{peak} = 2 \cdot F_{average}$. Since the particle is three orders of magnitude smaller than the laser beam, we can precisely calculate the incident laser fluence on a single AuNP. Therefore, direct correlation with the simulation results is feasible.

Figure 3a shows a series of time-resolved images of multiple successive PB generated around a single AuNP excited with a F_{peak} = 200 mJ/cm^2 fs laser irradiation at 10 Hz. A 2 ns frame-to-frame alteration of the pump-probe delay was applied to capture the PB dynamics in a time scale ranging from 1 ns to 50 ns. Notice that subsequent bubble images were captured for a single AuNP (i.e., always the same NP), which acted as a nanolens under successive fs laser pulses without any evidence of deformation or fragmentation. The corresponding movie of the PB dynamic evolution could be found in **supplementary video 2**. The presence of the PB was detectable even 1 ns after the fs excitation of the AuNP. Similar series of images were also captured for F_{peak} = 150 mJ/cm^2 and 250 mJ/cm^2. The PB life time, t_B, can be estimated using the approximate formulation $t_B \sim 2\, t_{R\,max}$, where $t_{R\,max}$ corresponds to the time, in which, the PB gains its maximum size. t_B was calculated to be 34 ± 3 ns, 40 ± 3 ns and 44 ± 3 ns for F_{peak} = 150 mJ/cm^2, 200 mJ/cm^2, and 250 mJ/cm^2, respectively. PB sizes were extracted by image processing and they are given in Figure 3b as a function of time and laser fluence. The maximum PB diameter was measured to be 1.1 ± 0.1 µm, 1.2 ± 0.1 µm and 1.4 ± 0.1 µm (mean ± s.d.) for F_{peak} = 150 mJ/cm^2, 200 mJ/cm^2, and 250 mJ/cm^2, respectively. These experimental values are in excellent agreement with those predicted in the recent analytical modeling work of Boulais et al.[11]. Due to the linear polarization of the incident light a slight bubble shape asymmetry in the growth phase has been proposed in the same work[11]. However, direct experimental demonstration of this effect was not possible with our imaging technique, possibly due to the lack of the required resolution. The shadowing in the bottom side of the PB pictures (Figure 3a) is due to not perfect alignment of the probe illumination. Notice that the optical system was implemented using an objective lens that compromises relatively high optical resolution (0.61 λ/NA ~ 650 nm) and sufficient depth of focus (~ 1 µm) to achieve dynamic imaging of the NB. In order to minimize uncertainty in PB size measurements only sharp PB images where processed (see experimental part).The latter had no effect on single AuNP/PB studies since tracking of individual particles was feasible for few tenths of seconds.

Based on the experimental results presented in Figure 3 we can extract the following relation between the t_B and the maximum diameter D_{max} of the examined PB : $t_B(ns) = (0.032 \pm 0.004)\, D_{max}(nm)$. The experimentally observed relation follows the linear Rayleigh formulation[25], $t_B(ns) \approx 0.092\, D_{max}$ (nm), presenting a 3-times smaller value for the linear term. However, there is a closer agreement (1.3-times smaller) considering the correction factor of ~ 2, proposed by Vogel et al.[19] for the Rayleigh formulation to include the dominant effect of the surface tension when D_{max} ~ 1 µm. It is worth to mention that in this simple D_{max} and t_B correlation based on Rayleigh model, we neglect the presence of the AuNP in the bubble and the slight asymmetry observed at the bubble growth and collapse time. Nevertheless, the experimentally observed correlation validates the reported single nanolens/PB imaging approach with an uncertainty as low as the experimental error.

It is mentioned that no bubble oscillation has been observed for the studied laser pulse energies. This is probably due to the strong dependence of the bubble oscillation damping terms on the bubble size[25,26]. Indeed, submicron-sized bubbles experience enormous oscillation damping due to liquid viscosity[26]. This probably resulted in a total suppression of the common oscillation behaviour, which is observed in a few microns sized bubbles[17]. Strong pressure wave propagation was predicted for off-resonance PB generation[11]. However,

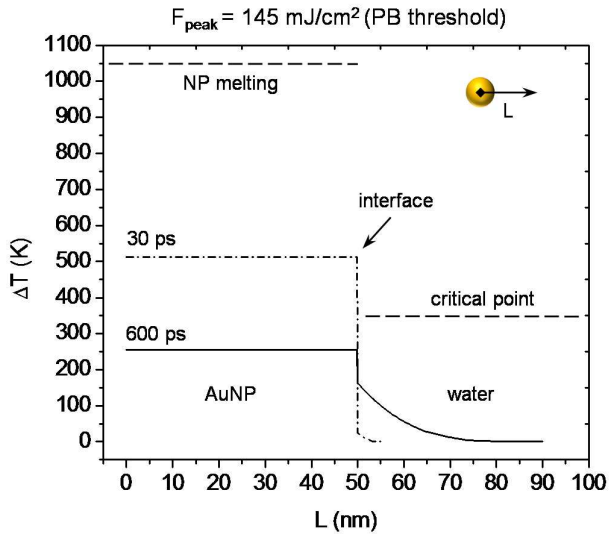

FIGURE 4 Calculated temperature profile as a function of the distance from the centre of the AuNP for F_{peak} = 145 mJ/cm^2 (bubble threshold). Two time frames of interest are presented: (i) 600 ps (i.e. maximum water temperature - solid line) and (ii) 30 ps (i.e., maximum AuNP lattice temperature - dashed line). The melting point of the 100 nm AuNP and the water critical point are also indicated in the graph with dashed lines.

pressure waves were not resolved around single AuNP in this set up because it would have require a much shorter probe pulse width.

COMSOL multiphysics simulations were employed to provide an insight to the nanocavitation mechanisms that governs the off-resonance fs laser excitation of plasmonic AuNPs in liquid. We calculated the temperature evolution in the 100 nm AuNP and around its vicinity under fs laser excitation at the experimental defined PB generation threshold (i.e., 145 mJ/cm^2) using the two-temperature model (TTM). Analytical description of the TTM can be found in the supplementary material of Ref.[11]. In agreement with our experimental methodology, which involves dynamic imaging of PBs in the center of the Gaussian beam, we considered peak laser fluence in our calculations. Figure 4 reveals that the maximum temperature increase at the water medium (water/AuNP interface) is ΔT = 164K, which corresponds to a maximum temperature of 457K, well below (~ 0.7$T_{w,cr}$) the water critical point for cavitation ($T_{w,cr}$ = 647 K). Therefore, heat conduction does not justify cavitation nucleation and bubble generation. It is mentioned that the surrounding water reaches its maximum temperature at a time delay of $\Delta t_{w,max}$ = 600 ps regarding to the peak of the Gaussian pulse. Furthermore, calculations show a maximum lattice temperature increase of ΔT = 512K in the AuNP for $\Delta t_{l,max}$ = 30 ps. Notice that the maximum AuNP temperature increase at the PB generation threshold lies well below (~ 0.6$T_{Au,m}$) the melting point of the 100 nm AuNP. Those observations reveal a relative "cold" PB generation process, in which, the fs laser excited AuNPs provoke cavitation without being subjected to phase change. The latter is in well agreement with our experimental observations, where single AuNPs have been dynamically imaged to generate multiple PB (>1000) without any evidence of fragmentation or cavitation efficiency loss.

Further discussion on the experimentally observed cavitation threshold can be based on the theoretical modelling proposed in our recent work[11]. Indeed, the irradiation of a single 100 nm AuNP with 800 nm (off-resonance) linear polarized light results in plasmon excitation and near field enhancement at the poles of the particle. The maximum near filed enhancement E/E_0 reaches the value of 4.4 at the pole of the AuNP, giving a rise to critical power density I_{cr} = 6.2 x 10^{13} W/cm^2 for the experimentally observed PB generation threshold. This is above the reported theoretical and the experimental values for the optical breakdown threshold of water for 800 nm ultrashort laser pulses[27], justifying plasma generation at the AuNP poles. The expansion of the nanoplasma and the relative pressure increase at the medium have been proposed to provoke cavitation instead of NP heating[11]. The experimentally measured cavitation threshold and the observed NP stability, clearly and directly confirm the proposed plasma mediated mechanism. Smaller spherical AuNPs, up to ~50 nm, can also be used to generate efficient nanocavitation upon off-resonance fs irradiation. In this work, we selected to study 100 nm AuNPs since they present sufficient scattering cross section for single particle dynamic imaging by DF monitoring.

On-resonance laser PB generation (life time 20 ns - 100 ns) has been extensively studied using short laser pulses at 532 nm. PB generation laser fluences were reported to vary from 18 mJ/cm^2 (20 ps, 60 nm AuNP)[28] to 360 mJ/cm^2 (0.5 ns, 90 nm AuNP)[18]. It is mentioned that PB generation using on-resonance laser pulses results in significant AuNP size reduction [18]. This is due to the AuNP cavitation mechanism, which is based on the NP heating. Despite the difference in the nanocavitation mechanism, our results indicate that off-resonance fs pulses result in similar PB dynamics compared to the on-resonance PB generation. In this context, the main advantages of using off-resonance fs pulses are (i) the use of laser irradiation with significantly longer penetration depth in tissue for *in vivo* applications (ii) the possibility to maintain the NP intact (see next section). On the other hand, since non-linear interactions require high peak laser power density provided by ultrashort laser pulses, short (ns) pulses are not efficient for off-resonance PB generation.

AuNP efficiency in multiple PB generation

In the second part of our work we investigated the efficiency of the AuNPs to generate multiple cavitation events under off-resonance fs laser excitation. The study has been performed in a single AuNP/nanolens approach to provide a direct investigation of their stability under multiple laser pulses**.** Figure 5a shows a series of images of multiple successive PBs generated around a single AuNP/nanolens excited with progressively increasing F_{peak} from 140 to 252 mJ/cm^2. A schematic representation of the experiment is depicted in Figure 5c. PB images were capture at a fixed delay of 20 ns. Up to ~ 240 mJ/cm^2, the PB size presented an almost linear dependence on F_{peak} (Figure 5b). However, a significant

fluctuation on the PB size was observed for laser fluences above that value. The last frame of Figure 5a is indicative of the absence of PB generation around the dynamically imaged AuNP. The latter, is due to partial and/or total deformation of the AuNPs following the off-resonance laser irradiation. Since the near-field is reduced with the AuNP size reduction, one partially deformed AuNP may generate several bubbles, up to the point that the near-field is not sufficient to generate nanoplasma and cavitation.

In order to investigate the observed PB size fluctuation we applied an *in-situ* DF imaging of the laser irradiated area by applying a pulse-to-pulse alteration of the laser fluence. This method offers an *in-situ* monitoring of the AuNP size reduction and AuNP elimination due to the strong dependence of the DF intensity (i.e., far-field scattering) on the NP size. A schematic representation of the experiment is depicted in Figure 5d, while Figure 5b presents the normalized DF intensity integrated across the central part of the laser irradiated area. The DF intensity plateau at low laser fluence is indicative of intact AuNPs, while the plateau at high laser fluence is indicative of the AuNP elimination. Small NP fragments present weak scattering properties, while totally eliminated NPs have no contribution to the *in-situ* DF signal. Therefore, the progressive DF decrease indicates partial AuNP deformation (size reduction) and/or AuNP elimination. We can evaluate the resolution of this *in-situ* approach by considering the dependence of the scattering intensity, I_{AuNP_sc}, on the diameter, D_{AuNP}, of the AuNPs. This can be expressed as $I_{AuNP\_sc} \sim D_{AuNP}^{4.3}$ using Mie theory calculations for D_{AuNP} ranging from 80 nm to 100 nm. As an indication, a 2 nm reduction (from 100 nm to 98 nm) in the AuNP size corresponds to a 9 % reduction in the scattering intensity. For comparison, in *in-situ* spectroscopic AuNP deformation analysis, a 2 nm reduction in AuNP size corresponds to 2 nm shift in the extinction spectra.

The observed fluctuation in the PB size for peak laser fluence ranging from 240 mJ/cm^2 to 270 mJ/cm^2 can be linked to the *in-situ* DF measurements. Indeed, the PB size fluctuation reflects the averaging of two competing trends on the PB size: (a) the generation of smaller PB due to AuNP size reduction and (b) the PB size increase with the increase of the laser fluence for intact NPs. The above analysis enables to accurately define an effective laser processing window, ranging from F_{peak} = 145 mJ/cm^2 to 240 mJ/cm^2, indicative of successive PB generation by intact plasmonic AuNPs/nanolenses. It is worth mentioning that we achieved detection of ~ 1000 successive PB generated by a single intact AuNP/nanolens when the laser fluence was set within the effective laser processing window. This number was limited by the detection method (i.e., the maximum time that the NPs remains traceable). Thus, the maximum number of successive PB could be considerably higher.

Those observations are of significant importance for NP-assisted laser nanosurgery applications were NP fragmentation should be prevented to avoid side effects such as cell necrosis and/or mitochondrial damage[29]. In fact, the observed effective processing window (F_{peak}: 145 mJ/cm^2 to 240 mJ/cm^2 or $F_{average}$: 73 mJ/cm^2 to 120mJ/cm^2) can be correlated with

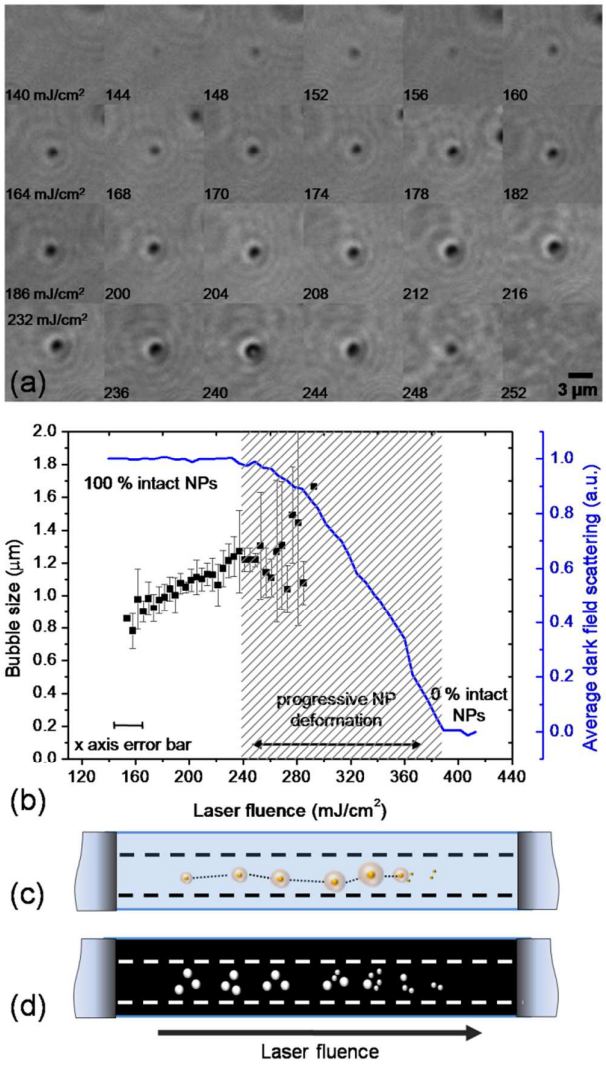

FIGURE 5 a) A series of time-resolved shadowgraphic images of successive bubbles generated by fs laser excitation of a single plasmonic AuNP at 20 ns delay. Images were captured at 10 Hz with a pulse-to-pulse increase of the peak laser fluence. Two dimensional movement of the particle was corrected by using image processing software. b) (left axis) Bubble diameter as a function of the peak laser fluence. The error bars correspond to the standard deviation of 5 events (i.e., complete dynamic tracking around 5 different NPs). (right axis) The average dark field intensity at the irradiated area as a function of the peak laser fluence. (c) and (d) show schematic representations of the measurements presented in right and left axis of the graph, respectively.

recent cell manipulation studies based on off-resonance excitation of AuNPs. Baumgart et. al.[24] reported optimum average laser fluence of 100 mJ/cm^2 for cancer cell transfection using off-resonance fs laser excitation of 100 nm AuNPs. Schomaker et. al.[30] reported 80 mJ/cm^2 as optimum average laser fluence for cell treatment using 250 nm AuNPs. Our results indicate that PB generated by single intact AuNPs can be generated under those conditions, which eventually play the key role for the cell membrane proration. Untargeted cells (no AuNP attached) remain intact under the reported processing window[24]. In future nanosurgery applications AuNP will be injected in-vivo and upon irradiation, the PB will induce

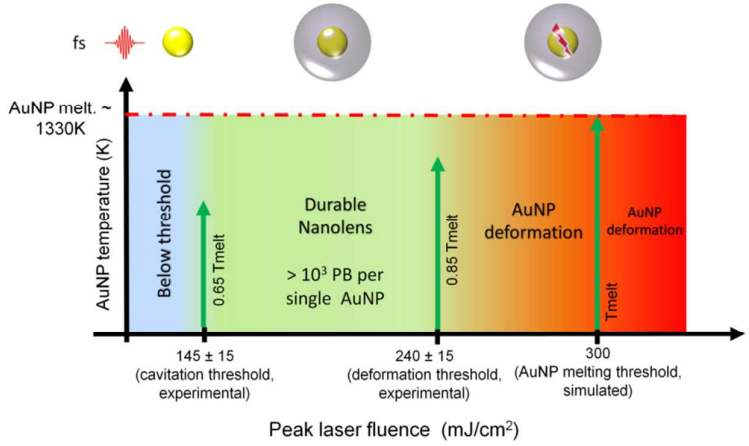

FIGURE 6 The observed AuNP nanolens effect in liquid is presented in diagram summarizing the experimentally defined nanocavitation and AuNP deformation thresholds. The simulated thermodynamic response of the AuNP is also indicated with arrows and compared with the AuNP melting point. Peak laser fluence is considered.

a localized treatment. The observed PB generation threshold is more than one order of magnitude lower than the reported optical breakdown thresholds for tissue (> J/cm^2) for 800 nm fs pulses[31,32]. Moreover, due to the single laser pulse driven PB cavitation mechanism, *in-vivo* heat accumulation and relative photothermal effects will be negligible. Therefore, non-targeted tissue is expected to remain unaffected for the reported laser fluences used.

Due to the conventional imaging methods employed so far, there are no relative studies dealing with direct observation of fs laser induced fragmentation of single NPs. However, spectroscopic NP extinction measurements have been extensively used to study NP fragmentation indirectly[33–35]. Using the *in-situ* DF imaging method we observed an almost two times lower AuNP fragmentation threshold compared to our previous observations based on a spectroscopic study of the NP extinction[24]. This difference can be explained by considering some inherent limitations associated with laser excitation and probing of a NP suspension in a container, i.e., (a) the difficulty to isolate the contribution of the non-irradiated NPs to the extinction signal and (b) the difficulty to ensure uniform irradiation of the entire NP suspension volume at the peak fluence of the focused Gaussian beam, which could lead to an overestimation of the AuNP fragmentation threshold[33].

We observed no AuNP aggregation within the reported processing window. Moreover, in relative in-situ spectroscopy measurements, no SPR peak change (broadening and/or shift) was found for off-resonance fs laser irradiation of AuNPs below the deformation threshold[24]. Those results suggest that the stabilizing organic shell (citrate) of the AuNPs remained functional after the PB generation.

In order to investigate the AuNP deformation mechanism we applied the TTM to calculated the maximum temperature increase, T_{lmax} = 1125K, in the AuNP for laser fluence equal to the experimentally observed NP deformation threshold, i.e., 240 mJ/cm^2. The calculated maximum lattice temperature is slightly below the melting point (~ 0.85 $T_{Au,m}$) of the AuNP ($T_{Au,m}$ = 1330K). Furthermore, we have calculated that AuNP melting occurs for laser fluences slightly higher at 300 mJ/cm^2, a value at which "partial" deformation occurs (see Fig. 5b). Considering that a simulation model gives reasonable values, but still includes assumptions[11], the calculated values are so close that it is difficult to get a firm conclusion on the predominant role of thermal destabilisation, evaporation and melting on the deformation mechanism. Alternatively, non-thermal NP deformation mechanisms, such as ejection of material from the NP poles due to near field enhancement[36] and Coulomb explosion[6], may play a role in NP deformation for laser fluences close to the deformation threshold at 240 mJ/cm^2. This must be further investigated.

Conclusions

In summary, we have examined directly cavitation and PB dynamics induced by off-resonance fs laser irradiation of plasmonic AuNPs, in a single NP approach, using a dynamic imaging method. The single particle approach revealed that a 100 nm AuNP can act as a durable nanolens in liquid, generating multiple submicron-sized PBs without any evidence of fragmentation for a wide laser processing window (Figure 6). Theoretical simulations provided an insight to the cavitation mechanism, which involves a critical nanoplasma generation at the poles of the NP due to near field enhancement at laser fluence well below the thermal destabilization threshold of the AuNPs. This unique ability of the AuNPs to provoke cavitation while remaining intact arises from the (a) appropriate off-resonance matching between the irradiation wavelength and the NP size and (b) the photoionization efficiency of the fs pulses. Our experimental observations are of significant importance towards *in-vivo* theranostic applications, where the proposed spatiotemporal match between the laser pulse and the AuNP size, not only provides well controlled PBs for therapy in the tissue therapeutic optical window (i.e., cancer treatment, gene delivery) but also ensures that the AuNP will remain intact. The

latter prevents cytotoxicity and allows for further sensing and imaging integration due to the preservation of the excellent optical properties of the AuNP probes.

Acknowledgements

CB acknowledges financial support from the Le Fonds de recherche du Québec. (post-doctoral scholarship (2012-2013)) and from the European Union (Marie Curie Fellowship FP7-PEOPLE-2013-I0F). The authors thank Rémi Lachaine for valuable discussions and Yves Drolet for technical support.

References

1 E. Boulais, R. Lachaine, A. Hatef and M. Meunier, *J. Photochem. Photobiol. C Photochem. Rev.*, 2013, **17**, 26–49.
2 D. Lapotko, *Cancers (Basel).*, 2011, **3**, 802–840.
3 E. Y. Lukianova-Hleb, M. B. G. Mutonga and D. O. Lapotko, *ACS Nano*, 2012, **6**, 10973–81.
4 C. Yao, R. Rahmanzadeh, E. Endl, Z. Zhang, J. Gerdes and G. Hüttmann, *J. Biomed. Opt.*, 2005, **10**, 064012.
5 C. M. Pitsillides, E. K. Joe, X. Wei, R. R. Anderson and C. P. Lin, *Biophys. J.*, 2003, **84**, 4023–32.
6 S. Hashimoto, D. Werner and T. Uwada, *J. Photochem. Photobiol. C Photochem. Rev.*, 2012, **13**, 28–54.
7 R. Lachaine, E. Boulais and M. Meunier, *ACS Photonics*, 2014, **1**, 331–336.
8 V. K. Pustovalov, a. S. Smetannikov and V. P. Zharov, *Laser Phys. Lett.*, 2008, **5**, 775–792.
9 E. Lukianova-Hleb, Y. Hu, L. Latterini, L. Tarpani, S. Lee, R. a Drezek, J. H. Hafner and D. O. Lapotko, *ACS Nano*, 2010, **4**, 2109–23.
10 D. Lapotko, *Opt. Express*, 2009, **17**, 2538–56.
11 E. Boulais, R. Lachaine and M. Meunier, *Nano Lett.*, 2012, **12**, 4763–9.
12 N. N. Nedyalkov, S. Imamova, P. A. Atanasov, Y. Tanaka and M. Obara, *J. Nanoparticle Res.*, 2011, **13**, 2181–2193.
13 E. Y. Lukianova-Hleb and D. O. Lapotko, *Appl. Phys. Lett.*, 2012, **101**, 264102.
14 R. Lachaine, E. Boulais, E. Bourbeau and M. Meunier, *Appl. Phys. A*, 2012, 1–4.
15 V. Kotaidis and A. Plech, *Appl. Phys. Lett.*, 2005, **87**, 213102.
16 V. P. Zharov, K. E. Mercer, E. N. Galitovskaya and M. S. Smeltzer, *Biophys. J.*, 2006, **90**, 619–27.
17 Y. Arita, M. Ploschner, M. Antkowiak, F. Gunn-Moore and K. Dholakia, *Opt. Lett.*, 2013, **38**, 3402–5.
18 E. Y. Lukianova-Hleb and D. O. Lapotko, *Nano Lett.*, 2009, **9**, 2160–6.
19 A. Vogel, N. Linz, S. Freidank and G. Paltauf, *Phys. Rev. Lett.*, 2008, **100**, 038102.
20 E. Y. Lukianova-Hleb, E. Y. Hanna, J. H. Hafner and D. O. Lapotko, *Nanotechnology*, 2010, **21**, 85102.
21 A. M. Alkilany and C. J. Murphy, *J. Nanopart. Res.*, 2010, **12**, 2313–2333.
22 F. Tournus, *J. Nanoparticle Res.*, 2011, **13**, 5211–5223.
23 C. Boutopoulos, M. Fortin-Deschênes, E. Bergeron and M. Meunier, in *SPIE Frontiers in Ultrafast Optics: Biomedical, Scientific, and Industrial Applications XIV*, eds. A. Heisterkamp, P. R. Herman, M. Meunier and S. Nolte, 2014, vol. 8972, p. 897208.
24 J. Baumgart, L. Humbert, É. Boulais, R. Lachaine, J.-J. Lebrun and M. Meunier, *Biomaterials*, 2012, **33**, 2345–50.
25 Christopher E. Brennen, *Cavitation and Bubble Dynamics*, Oxford University Press, New York, 1995, vol. 4.
26 R. B. Chapman and M. S. Plesset, *J. Basic Eng.*, 1971, **93**, 373–376.
27 A. Vogel, J. Noack, G. Hüttman and G. Paltauf, *Appl. Phys. B*, 2005, **81**, 1015–1047.
28 E. Y. Lukianova-Hleb, A. N. Volkov and D. O. Lapotko, *Langmuir*, 2014, **30**, 7425–7434.
29 Y. Pan, A. Leifert, D. Ruau, S. Neuss, J. Bornemann, G. Schmid, W. Brandau, U. Simon and W. Jahnen-Dechent, *Small*, 2009, **5**, 2067–76.
30 M. Schomaker, D. Killian, S. Willenbrock, D. Heinemann, S. Kalies, A. Ngezahayo, I. Nolte, T. Ripken, C. Junghanß, H. Meyer, H. M. Escobar and A. Heisterkamp, *J. Biophotonics*, 2014, **in press**, doi: 10.1002/jbio.201400065.
31 P. S. Tsai, P. Blinder, B. J. Migliori, J. Neev, Y. Jin, J. A. Squier and D. Kleinfeld, *Curr. Opin. Biotechnol.*, 2009, **20**, 90–99.
32 F. H. Loesel, M. H. Niemz, J. F. Bille and T. Juhasz, *IEEE J. Quantum Electron.*, 1996, **32**, 1717–1722.
33 S. Hashimoto, D. Werner and T. Uwada, *J. Photochem. Photobiol. C Photochem. Rev.*, 2012, **13**, 28–54.
34 O. Warshavski, L. Minai, G. Bisker and D. Yelin, *J. Phys. Chem. C*, 2011, **115**, 3910–3917.
35 D. Werner, A. Furube, T. Okamoto and S. Hashimoto, *J. Phys. Chem. C*, 2011, **115**, 8503–8512.
36 A. Plech, V. Kotaidis, M. Lorenc and J. Boneberg, *Nat. Phys.*, 2005, **2**, 44–47.